

The emission measure distribution of impulsive phase flare footpoints

D.R. Graham¹, I.G. Hannah¹, L. Fletcher¹ and R. O. Milligan²

School of Physics and Astronomy, University of Glasgow, G12 8QQ, UK.

Astrophysics Research Centre, School of Mathematics and Physics, Queens University Belfast, Belfast, BT7 1NN, UK.

d.graham@astro.gla.ac.uk

ABSTRACT

The temperature distribution of the emitting plasma is a crucial constraint when studying the heating of solar flare footpoints. However, determining this for impulsive phase footpoints has been difficult in the past due to insufficient spatial resolution to resolve the footpoints from the loop structures, and a lack of spectral and temporal coverage. We use the capabilities of *Hinode*/EIS to obtain the first emission measure distributions (EMDs) from impulsive phase footpoints in six flares. Observations with good spectral coverage were analysed using a regularized inversion method to recover the EMDs. We find that the EMDs all share a peak temperature of around 8 MK, with lines formed around this temperature having emission measures peaking between 10^{28} and 10^{29} cm⁻⁵, indicating a substantial presence of plasma at very high temperatures within the footpoints. An EMD gradient of $EM(T) \sim T$ is found in all events. Previous theoretical work on emission measure gradients shows this to be consistent with a scenario in which the deposited flare energy directly heats only the top layer of the flare chromosphere, while deeper layers are heated by conduction.

Subject headings: Sun: activity - Sun: chromosphere - Sun: flares - Sun: transition region - Sun: UV radiation - Sun: X-rays, gamma rays

1. Introduction

A clear observational description of the plasma properties of the lower atmosphere footpoints of solar flares provides a critical constraint on the distribution of the flare excess energy in this region, and hence the profile of flare energy deposition and its possible modes of transport. The emission measure distribution (EMD) is a way to describe the amount of emitting plasma as a function of its temperature, and in this paper we present the first determination of impulsive phase flare footpoint EMDs made using the Extreme Ultraviolet Imaging Spectrometer (EIS, Culhane et al. 2007) onboard the *Hinode* satellite. The temperature coverage of EIS makes it extremely well suited to studying the properties of footpoints during flares, where impulsive stage temperatures can be very

high - on the order of 8-10 MK, but present in the lower atmosphere during the extreme conditions of a flare.

There have been several previous studies of the distribution of emission measures of solar flares. For example, EUV data from the Skylab NRL slitless spectroheliograph enabled spatial as well as spectral information to be deduced, though the “overlappograms” produced convolved spatial and spectral information leading to source confusion. Several flare EMDs from the rise and decay phases have been published from this instrument. The EMD of Dere et al. (1977), from just before the peak of the 0.5-3 Å rise phase of flare SOL1973-09-05T18:32¹, which would correspond roughly to

¹we use the solar observation target identification convention described by Leibacher et al. (2010)

the end of the impulsive phase, had a steep slope up to a peak at $\log T \sim 6.9$. There was evidence for emission at Fe XIV to Fe XVI at concentrated footpoints or near the ends of loops, as well as in loops themselves.

The distribution of emission measures² found in the impulsive phase of a flare by Widing (1982) in SOL1973-12-22T00:24 had slope $\int n_e(T)^2 dS \sim T^{0.8}$ from $\log T = 5.4$ up to $\log T = 6.2$, with the suggestion of a decrease above $\log T \sim 6.9$. Here, n_e is the electron number density and S the distance along the line of sight. Widing & Hiei (1984) presented emission measure distributions from two compact flare sources just after the impulsive peak of SOL1974-01-21T23:24, one of which had a shallow slope (scaling as $T^{0.6}$) up to a maximum at $\log T \sim 6$, and the other had a slope of 3 up to $\log T \sim 6.9$. Widing (1982) emphasizes that these slopes are different from the $3/2$ slopes which are often assumed to be characteristic of flares. Other observations have been obtained during decay phases of flares (Dere & Cook 1979; Widing & Spicer 1980), and have also tended to attract more theoretical attention (Machado & Emslie 1979).

High densities in impulsive-phase sources were also found using the Skylab data, including in high temperature lines (Doschek et al. 1977; Feldman et al. 1977). Related observations from the *Yohkoh* satellite (Acton et al. 1992) have also shown high temperatures and densities during the impulsive phase, and more specifically soft X-ray emission from the footpoints (McTiernan et al. 1993; Hudson et al. 1994; Mrozek & Tomczak 2004). High footpoint temperature and density observations have recently been amply confirmed by EIS (e.g. Milligan 2011; Del Zanna et al. 2011; Graham et al. 2011; Watanabe et al. 2010).

In this paper, we are able to isolate the footpoints in six flares, and determine their impulsive phase EMDs using EIS. The $\sim 4''$ spatial resolution of EIS is sufficient to make a clear identification of footpoints and loops, based on their

morphology at different wavelengths. We identify six flares having consistent spectral coverage and raster observations during their impulsive phases. The EMDs recovered are remarkably consistent with one another, peaking at a temperature of $\log T \sim 6.9$, at a maximum value of $10^{28} - 10^{29} \text{ cm}^{-5}$ and with EMDs below the peak temperature characterized by $EM(T) \sim T$.

Section 2 details the EIS data reduction, while an overview of the flare observations and their selection is found in Section 3. Section 4 describes the inputs required in calculating the DEM and the regularized inversion method used to determine the DEM. The footpoint EMDs are shown in Section 5 and discussed in depth in Sections 6 and 7.

2. EIS Observations

To obtain EMDs of flare footpoint plasma we require observations of flares during the impulsive (rise) phase at multiple temperatures, ideally in emission lines given their narrow sensitivity to temperature (see Section 4). Its spatial, temporal, and spectral capabilities make *Hinode*/EIS well suited for this task. The spectrometer slit can be scanned across the area of an active region multiple times during the flare, building up raster “images” in many wavelengths simultaneously. Good datasets for flare footpoint studies are hard to find. Positioning the slit over the small footpoints (typically 2-5'') early in the flare is not always possible, and since March 2008 telemetry from the *Hinode* spacecraft has been limited, restricting the temperature sampling.

Flare observations using the EIS raster study CAM_ARTB_RHESSI_b_2 fulfilled our requirements and six were selected. These use the 2'' slit to scan a 40'' x 140'' area in 3 min 52 s. Around 30 lines are present in these rasters but we have narrowed the selection down to 15 to best cover the temperature range (Figure 1), and avoid density-sensitive or optically thick lines. Line details are listed in Table 1 and contribution functions in Figure 1. All of the data has been calibrated and fitted using the standard EIS_PREP and EIS_AUTO_FIT SolarSoft routines. An exception is the analysis of Ca XVII which uses the method described below. We also correct for a measured 17'' North-South and 1'' East-West offset between

²A distinction should be made here between the EMD and *differential* emission measure (DEM). The DEM $\xi(T)$ is the quantity of units $\text{cm}^{-5} \text{ K}^{-1}$ derived from an inversion of the data, e.g. via the method described in Section 4. Integrating the DEM over a fixed logarithmic temperature interval gives the emission measure as a function of temperature $EM(T)$ in the more practical units of cm^{-5}

the two separate wavelength bands on the instrument's CCD.

Table 1: Emission lines selected for EMD analysis with rest wavelengths and peak formation temperatures.

Ion	λ (Å)	$\log_{10} T$ (K)
O V	248.460	5.4
O VI	184.118	5.5
Fe VIII	185.213	5.7
Mg VI	268.991	5.7
Si VII	275.361	5.8
Fe X	184.537	6.1
Fe XI	188.216	6.2
Fe XII	195.119	6.2
Fe XIII	202.044	6.3
Fe XIV	274.204	6.3
Fe XV	284.163	6.4
Fe XVI	262.976	6.4
Ca XVII	192.853	6.8
Fe XXIII	263.766	7.2
Fe XXIV	192.028	7.2

We extract for each emission line the fitted integrated line intensity averaged over a $2'' \times 3''$ area around a footpoint (1×3 pixels) centred on the pixel brightest in Fe VIII. The strongest footpoint emission in these events mostly appears over one slit position $2''$ wide. To bin further in the x -direction would sample too much of the surrounding area, thus our binning accounts for the spatial extent of the footpoint and covers some offset between wavelengths.

A pre-flare background was not subtracted from the footpoint emission. This allows us to make consistent comparisons with the EMDs described in the introduction, and the theoretical work discussed in Section 6; which treats emission from the entire emitting column, not only the flare excess.

A number of the lines selected are blended by neighboring transitions, however the true intensities can be recovered using fitting techniques and other observed lines within the raster. The CHIANTI v7.0 atomic database (Dere et al. 1997; Landi et al. 2012) is used to identify lines contributing to the measured line profiles.

The low temperature Fe VIII 185.213 line has two reported blends of Ni XXIV 185.166 and Ni

XVI 185.230. Fitting with three Gaussians reveals small 10-20% blue wing contributions of Ni XXIV 185.166 around, but not necessarily within, the footpoints. In the red wing CHIANTI predicts Ni XVI 185.230 to be the stronger contribution, however, no obvious third Gaussian could be seen from our fitting and so Ni XVI should not have a significant effect on the Fe VIII intensity.

Fe XXIV 192.028 normally dominates in flare loop conditions and contributions from blends of Fe VIII and Fe XI are small. This work concentrates on an earlier phase in the flare where the Fe XXIV emission will be much fainter, therefore a significant Fe XI 192.021 contribution must be removed. We do this via the method described in Del Zanna et al. (2011). The observed Fe XI 201.734 intensity forms a known ratio with $\lambda 192.021$, this can then be used to estimate the $\lambda 192.021$ intensity in the footpoint. We find the ratio of 192.021/201.734 in background moss/active regions to be 0.43. The Fe VIII 192.004 intensity is predicted by CHIANTI to be around 10% of the Fe XI line and is almost negligible. Accounting for these contributions removes most of the active-region emission (seen in Figure 3) leaving a mean background level lower than the line uncertainties (see Section 4.1 on DEM uncertainties).

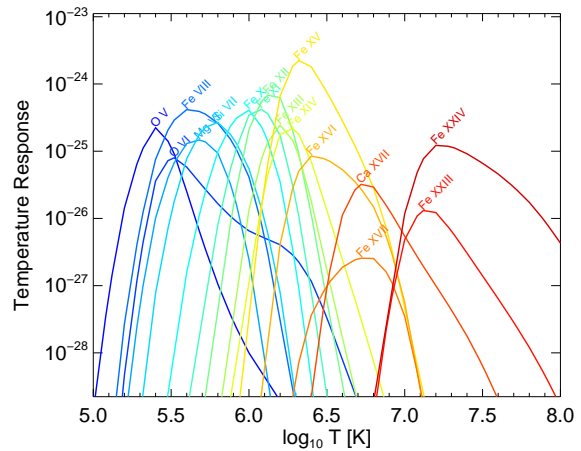


Fig. 1.— Contribution functions $G(T)$ for emission lines calculated with coronal abundances, CHIANTI's own ionization equilibrium file, and a constant density of 10^{11} cm^{-3}

Ca xvii 192.853 forms part of a complex grouping of six O v and two Fe xi lines, therefore interpretation of the line is challenging but is well documented (Ko et al. 2009; O’Dwyer et al. 2010; Del Zanna et al. 2011) and we have adopted the approach in Ko et al. (2009) to estimate the Ca xvii intensity. First the two Fe xi 192.813/192.901 intensities are estimated using known ratios to Fe xi 188.216. In most of the footpoints the strong density sensitive O v 192.904 line can be resolved and the other five O v lines are estimated from CHIANTI v7.0 using a fixed density of 10^{11}cm^{-3} .

3. Flare Observations and Footpoint Selection

Six events, varying in GOES class from B1.8 to C1.1, were selected from a period between May and December 2007 (Figure 2). Two of the six events labeled Event (b) (SOL2007-12-14T14:16:30) and Event (f) (SOL2007-05-22T23:25:50) have been examined in greater detail; Event (b) by Milligan & Dennis (2009) and Milligan (2011) — on the subject of non-thermal line broadening, and Event (f) by Del Zanna et al. (2011). These events are observed to exhibit footpoint EUV and HXR emission, chromospheric evaporation, and footpoint electron density enhancements.

Rasters shown in Figure 3 illustrate the flare appearance at 500,000 K (Fe viii) and at 16 MK. (Fe xxiv). From the work by Milligan & Dennis (2009) and Graham et al. (2011), compact brightenings in transition region lines can often be associated with RHESSI HXR observations revealing the flare energy deposition site. Rasters have been selected where compact, co-spatial Fe viii and Fe xxiv emission rises dramatically compared to the background. Figure 3a (Event (a)) shows small bright sources appearing in Fe viii during the rise phase. Compact, hot Fe xxiv emission is also present at this early stage but becomes more significant later as evaporating hot material begins to fill loop structures. Figure 3b, (Event (b)) is sampled slightly later in the impulsive phase and shows a hot flare loop forming next to the footpoint.

These events are highly impulsive. GOES lightcurves for each event in Figure 2 show that

the rise phase of most events lasts 2-4 minutes, with the longest just under 10 minutes. Typically HXR observations are used to verify that the EUV emission corresponds to the impulsive phase. However, RHESSI HXR data were not consistently available, and so we systematically use the GOES derivative as a proxy for the HXR emission (Neupert 1968); a dashed line on the lightcurves marks where this peaks and is used as a guide to select EIS rasters during the impulsive phase. In each event at least one EIS raster was found spanning part or all of the impulsive phase. Rasters have been chosen as early as possible in the flare whilst still showing strong EUV enhancements, and keeping the GOES derivative peak within the chosen raster limits (dotted lines Figure 2). The flare evolves as the spectrometer slit scans right to left over the window. The time at which the slit crosses a footpoint is marked by a diamond on the lightcurve.

Given this morphology throughout the EIS temperature range, plus supporting wide field of view imaging from the X-Ray Telescope (XRT) onboard *Hinode* (Golub et al. 2007) and TRACE (Handy et al. 1999) (omitted here for space constraints), we are confident in identifying the flare footpoints, as marked with white arrows in Figure 3.

4. DEM Technique

The set of line observations, I_λ , and corresponding contribution functions, $G_\lambda(T, n_e)$, are related to the differential emission measure of the plasma via $I_\lambda = \int G_\lambda(T, n_e) \xi(T) dT$ where the DEM is defined as $\xi(T) = n_e^2(dS/dT)$. Obtaining $\xi(T)$ from I_λ is an “ill-posed” inverse problem, with uncertainties in the data resulting in the solution being non-unique. However, using physical constraints on the data can help recover a useful solution. There are a variety of techniques to recover the DEM (c.f. Fludra & Sylwester 1986; Monsignori Fossi & Landini 1991) with a Markov chain Monte Carlo (MCMC) approach being routinely adopted for spectral line data inversion (Kashyap & Drake 1998). In this paper we use a regularized inversion method (Hannah & Kontar 2012), which is able to produce solutions similar to the MCMC approach but is computationally quicker and estimates both horizontal and verti-

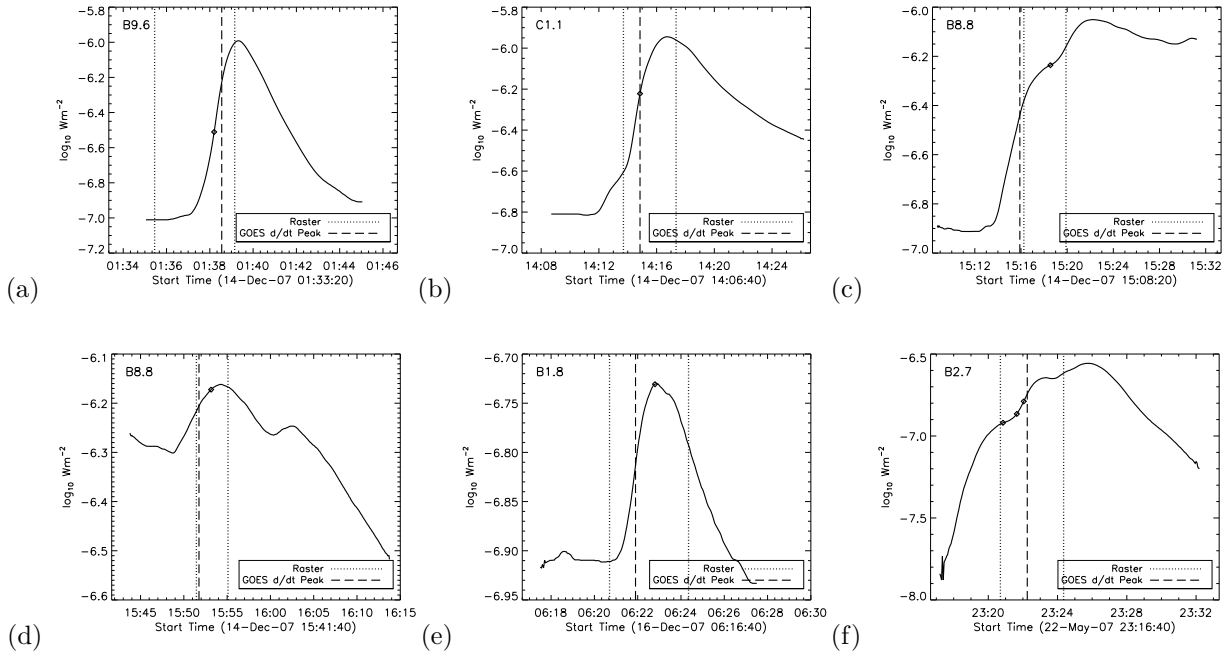


Fig. 2.— GOES 1-8Å lightcurves of each event. A pair of dotted vertical lines represent the start and end times of the EIS raster and a single dashed line marks the GOES derivative maximum for the event. The time at which the spectrometer slit scans each footprint is marked with a diamond on the light curve.

cal errors on the DEM solution. Regularization adds a “smoothness” constraint to the DEM solution so that a stable inversion can be recovered, avoiding amplification of the uncertainties (Tikhonov 1963). However, this may be a strong assumption. For example, the DEM of a loop in conductive equilibrium theoretically has a discontinuous, high temperature cut-off. The minimum of the EM loci curves (the curves representing the isothermal emission in each line) are used as an initial guess DEM solution. A multi-thermal DEM solution must be below these EM loci curves (since the isothermal solution gives the maximum possible emission at that temperature) and the regularized solutions achieve this (see Figure 4). The approach iterates until a positive DEM is found and also minimizes the chi-squared between the measured and regularized line intensities. For a full explanation of this approach on EIS line data compared to the MCMC method see Hannah & Kontar (2012).

4.1. DEM Inputs and Uncertainties

Determination of the DEM requires three inputs; line intensities, intensity error estimates, and the line contribution functions, here calculated using CHIANTI v7.0. These are calculated using coronal abundances (Feldman et al. 1992), CHIANTI’s own ionization equilibrium file (Landi et al. 2012) and a constant density of 10^{11}cm^{-3} suitable for flare footpoints (see e.g. Watanabe et al. 2010; Graham et al. 2011; Milligan 2011). The DEM shape should not be strongly affected by density variations, as the density-sensitive lines have been removed from the analysis. We assume a 20% systematic error across all intensity measurements to account for the absolute calibration uncertainty between lines (P. Young, private communication) and this is added to the fitting error.

It is difficult to determine the correct elemental abundances for use in flare analysis (Athay 1994; Feldman et al. 2004). In the standard model, footpoint material originates low in the chromosphere before being heated to coronal temperatures, yet

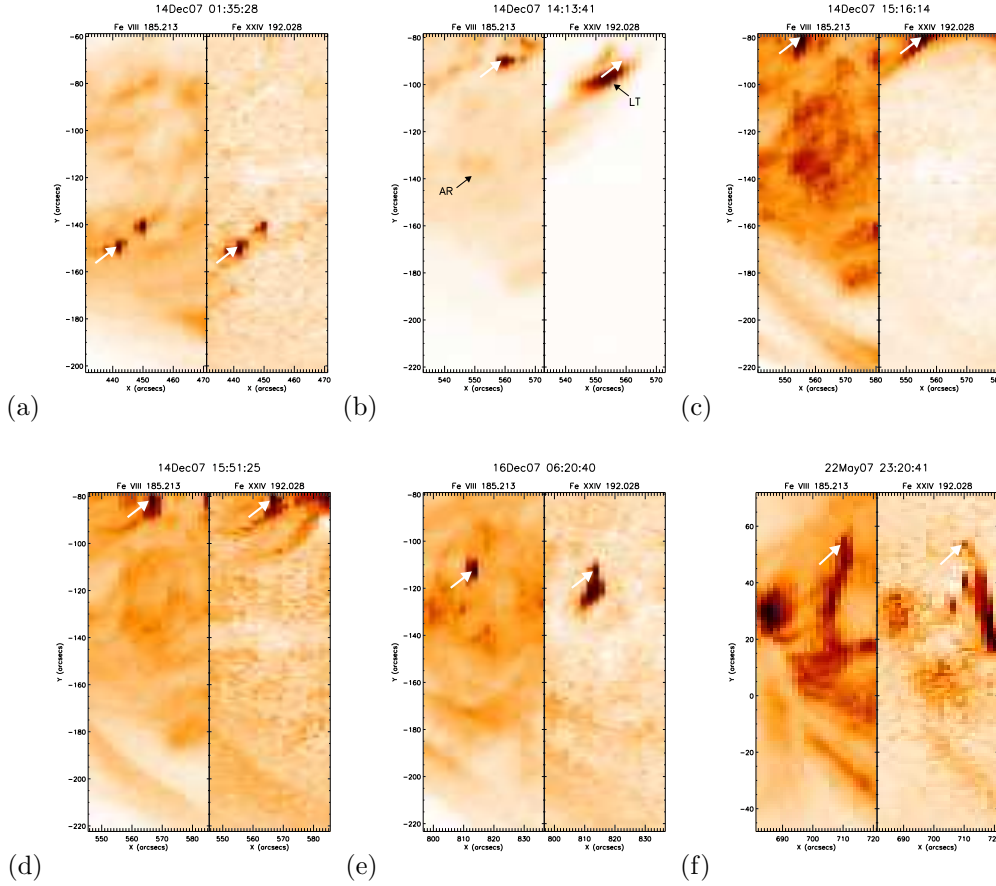


Fig. 3.— EIS rasters for each event in Fe VIII at 500,000K and Fe XXIV at 16 MK showing the morphology at low and high temperatures. A white arrow marks the footpoint positions chosen for EMD analysis in each raster. Black arrows in panel (b) also highlight the regions used in determining a loop top and active region EMD (see Section 6).

this material rises and mixes with existing coronal material in loops. The choice of abundances used to interpret flare spectra is therefore not straightforward. Furthermore, low FIP (first ionization potential) elements are found to be enhanced in coronal material compared to the photosphere while high FIP elements are unchanged. Only O V and O VI in our analysis are high FIP. The choice of ionization equilibrium is similarly uncertain. We will investigate the effects of varying abundance and ionization equilibrium in Section 5.1

4.2. Assumptions

Before interpreting spectra with CHIANTI one must be aware of the built-in assumptions. The $G(T)$ functions are calculated for an optically thin plasma in thermal and ionization equilibrium. Clearly from RHESSI HXR observations flare footpoint electron spectra have an inherently non-Maxwellian component of the electron distribution, although this can be small compared to the total energy of the distribution; see Krucker et al. (2011). In addition the footpoint is a location of intense heating, so it is possible to assume that the plasma is out of thermal and ionization equilibrium. However, the high density of

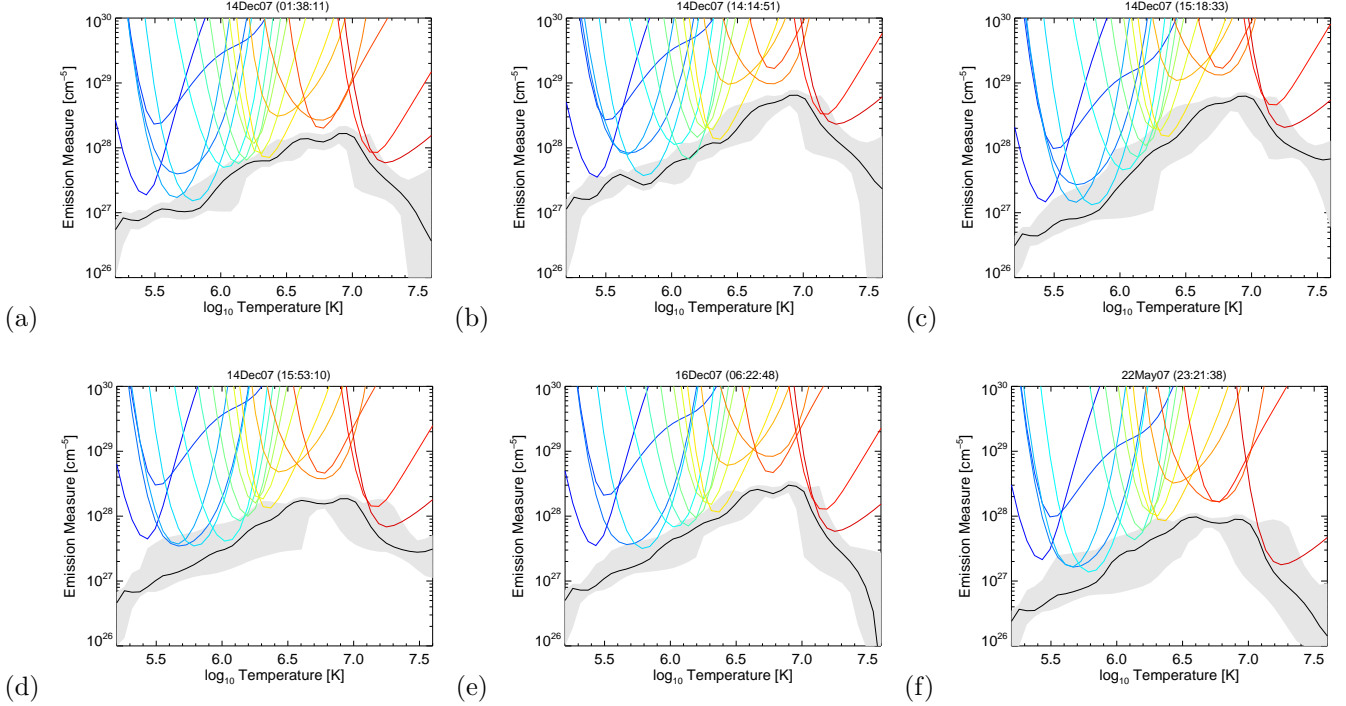


Fig. 4.— DEMs shown in black for each event in emission measure units cm^{-5} and the uncertainty limits of the solution by a shaded grey area. The colored curves show measured line intensity divided by the contribution function indicating the maximum possible emission, i.e. the EM loci curves.

the emitting region may provide a high enough electron collision rate for the footpoint plasma to be close to equilibrium. For a plasma at 10^6 K and $n_e = 10^{11} \text{ cm}^{-3}$ the electron-electron collision timescale is $\tau_{ee} = 1.33 \times 10^{-4} \text{ s}$, which is probably much shorter than the flare heating timescale, so the core electrons of the distribution can rapidly reach thermal equilibrium.

Calculation of non-equilibrium ionization (NEI) states by Bradshaw (2009) shows that during heating the population of a given ion peaks at a higher temperature than that at which it would peak in equilibrium. This could lead to systematically lower temperatures being inferred. Again the effect is more pronounced at lower densities as ionization and recombination processes are driven by electron collisions. Bradshaw (2009) finds that at densities of 10^{10} cm^{-3} the peaks can shift by up to $\log T = 0.3$ K but by $n_e = 10^{12} \text{ cm}^{-3}$ the difference is negligible.

Finally we assume that the plasma is optically thin. This may at first sight be a more problem-

atic assumption given the high densities and footpoint emission originating from deeper regions of the atmosphere, which may be optically thick. We estimate the opacity for Fe VIII, Fe X and Fe XVI from the method in Bloomfield et al. (2002) and Milligan (2011). The optical depth at line centre, τ_0 can be expressed as

$$\tau_0 = 1.16 \times 10^{-14} \lambda f_{ij} \sqrt{\frac{M}{T}} \frac{n_{ion}}{n_{el}} \frac{n_H}{n_H} \frac{N_e}{N_e} h \quad (1)$$

where λ is the line wavelength, f_{ij} the oscillator strength of the transition, and M the mass of the ion. n_{ion}/n_{el} and n_H/N_e are taken from the default CHIANTI ionization equilibrium file and coronal abundances. Taking a path length of $1''$ and $n_H = 5 \times 10^9 \text{ cm}^{-3}$ we find $\tau_0 = 0.527, 0.06$ and 0.04 respectively for Fe VIII, Fe X and Fe XVI. As expected emission lines at higher temperatures are largely unaffected by the plasma opacity, yet the cooler Fe VIII line may be influenced. An optical depth of $\tau_0 = 0.527$ corresponds

to a drop in transmission of $\sim 40\%$ — compared to the line uncertainty of at least 20% this could be significant. However, if photospheric abundances are used this drops to $\sim 10\%$, demonstrating that a careful analysis of flare abundances is required in future. To fully understand the effects of non-equilibrium and radiative transfer in a flare atmosphere is a serious undertaking which lies beyond the scope of this paper. Our results are the first of their kind using the best spectroscopy and atomic calculations available, but we must be aware of these possible shortcomings.

5. Flare EMDs

EMDs derived for the six different events using the above methods are shown in Figure 4. The figures show the emission measure distribution $EM(T)$ in units of cm^{-5} found by integrating the DEM over a fixed logarithmic temperature interval. This returns an EMD of the same form as those discussed in the introduction. In all events the EMDs in black lines are bounded by the colored EM loci curves, confirming that the regularized solutions are below the expected maximum emission.

A shaded region outlines the extent of the EMD uncertainty in temperature and EM space. The true solution lies within this boundary. Within the plotted temperature range the uncertainties in temperature are mostly within an order of magnitude or less in EM. At temperatures above 10^7 K the solutions have a large uncertainty due to the broad $G(T)$ response in Fe XXIII and Fe XXIV. Also these emission lines are fainter at footpoints so have larger fitting errors. Unsaturated, soft X-Ray observations from *Hinode*/XRT would have helped constrain this part of the EMD but were unavailable. Extending the temperature range beyond the limits of the $G(T)$ functions significantly spreads out the errors at the temperature limits. The regularization is unable to find solutions where $G(T)$ is undefined, hence it is therefore not possible to make physical conclusions beyond these limits.

All of the footpoint EMDs share a strikingly similar profile: increasing with an almost constant gradient of $EM(T) \sim T$ to a peak around $\log T = 6.9$ then falling off quickly at higher temperatures. The peak temperature suggests a sig-

nificant presence of plasma at 8 MK in the flare footpoints. Peak emission measures vary between 10^{28} and 10^{29} cm^{-5} but do not appear strongly related to the GOES class, which is perhaps expected for a small sample of lower energy events sampled at slightly different times in their evolution (see Table 2).

We measure a gradient of $EM(T) \sim T^{0.97 \pm 0.27}$ between $\log T = 5.5 - 6.9$ in Event (b), where the uncertainty is estimated by the maximum and minimum gradients allowed within the EMD error region. This footpoint EMD is plotted in Figure 5 (green region) against a line of gradient $EM(T) \sim T$ resembling our event, and $EM(T) \sim T^{\frac{3}{2}}$, a commonly observed gradient for a transition region/low corona atmosphere.

To verify that the similarity of the footpoint EMDs is not an artefact of the regularization method used, we have calculated EMDs from both active region (AR) and flare loop top (LT) plasma. Again using Event (b), EMDs from AR and LT locations are shown in Figure 5 in the orange and blue regions respectively, with the footpoint shown in green. The AR and LT locations on the raster are marked for reference by black arrows on Figure 3b. Their EMDs are noticeably different from the footpoint EMD, showing that the regularization responds well to different plasma temperature distributions. The active region EMD peaks between $\log T = 6.3 - 6.5$ with a lower emission measure and steep high temperature cut-off. The gradient in the AR and LT EMDs are steep ($> T^{\frac{3}{2}}$) and remarkably similar up to $\log T = 6.3$ where the loop top EMD becomes shallower and continues rising to over 10 MK — the point at which the EMD becomes poorly constrained.

Emission in the footpoint between temperatures of $\log T = 5.2 - 6.2$ is greater by up to an order of magnitude than in the active region or loop top. From the conventional understanding of flares it is likely this is chromospheric plasma in the process of being heated to flare temperatures. The break in similarity between the LT and AR gradients at $\log T = 6.3$ suggests that only plasma above this temperature is being evaporated into the flare loop, agreeing with the results in Milligan & Dennis (2009) where only footpoint plasma above $\log T = 6.2$ exhibits evaporative up-flows. A full flow velocity analysis will be the subject of future work, but it is reassuring to see that

such arguments can be made from the results and that the behaviour of the EMDs varies in reasonable ways across the event.

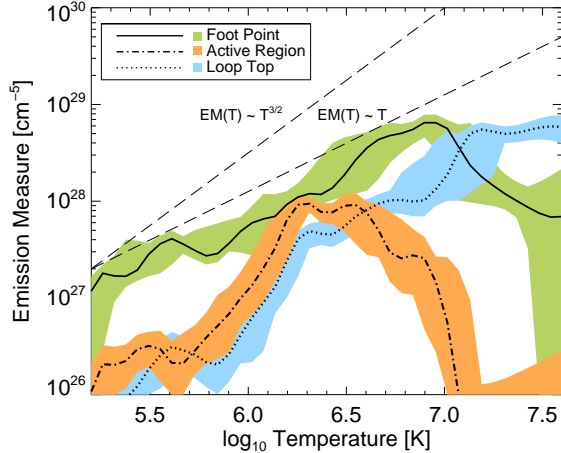


Fig. 5.— A comparison of footpoint, loop, and active region EMDs in Event (b). The purpose of this is to check the regularization response to different temperature distributions. Gradients of $EM(T) \sim T$ and $EM(T) \sim T^{3/2}$ are added in dashed lines.

5.1. Varying the abundance and ionization equilibrium

As discussed in Section 4.1, the appropriate values of abundance in the chromospheric plasma, and of the ionization equilibrium, are not known, therefore we repeat the analysis using various ionization files with photospheric and coronal abundances (Grevesse & Sauval (1998) and Feldman et al. (1992) respectively). EMD curves for the footpoint in Event (b) are shown in Figure 6 using photospheric (light shading) and coronal (dark shading) abundances. The EMD is around a factor of 4-5 larger using photospheric abundances but varies very little in shape; only at very low temperatures where oxygen is dominant is there any deviation in gradient. Changing the abundances therefore only alters the result significantly by a constant factor in EM, i.e. the gradient remains $EM(T) \sim T$ between $\log T \sim 5.5 - 6.9$.

Looking again at Figure 6 changing the ionization equilibrium parameters (solid, dashed, and dotted line styles) also has very little effect on the

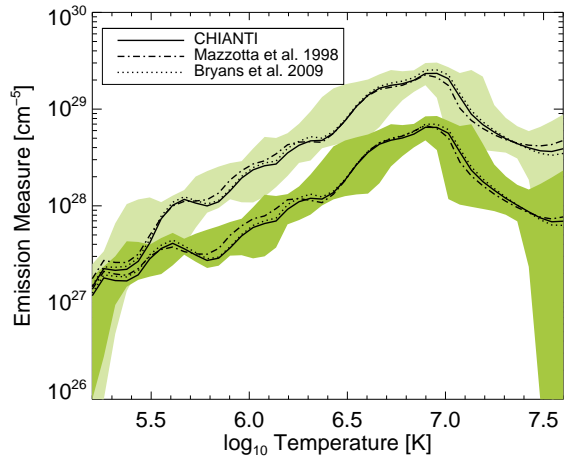


Fig. 6.— Footpoint EMD of Event (b) using photospheric and coronal abundances and a variety of ionization equilibrium theories (Landi et al. 2012; Mazzotta et al. 1998; Bryans et al. 2009). EMDs are shown by the black lines within a shaded error boundary. Curves within the lighter shaded area are from photospheric abundances and the darker from coronal abundances. For each abundance file three ionization equilibrium theories are tested and plotted in different line styles.

EMD. Given the large number of lines and small variations these parameters produce on the contribution functions, the final EMD is relatively insensitive, especially when considering how much larger the intensity uncertainties are. Any differences due to different ionization equilibria all lie within the error boundaries plotted.

5.2. Column emission measures

Estimating the emission measure of emitting plasma can also be approached through the use of density-sensitive line ratios. Milligan (2011) used five line ratios available in these rasters (Mg VII, Si X, Fe XII, Fe XIII, and Fe XIV) to estimate the footpoint electron density at various temperatures in Event (b), and from these and the observed intensities, calculate the respective column depths of the emitting material. Here we use these measurements of column depth for an alternate estimate of the column emission measure at a range of temperatures.

The intensity of a given emission line, I , inte-

Table 2: Event EMD parameters sorted by GOES Class.

Flare ID	GOES Class	Event	Peak Temp $\log_{10} T$ (K)	Peak EM $\times 10^{28} \text{cm}^{-5}$
SOL2007-12-16T06:22:40	B1.8	(e)	6.9	4.0
SOL2007-05-22T23:25:50	B2.7	(f)	6.9	1.0
SOL2007-12-14T15:22:00	B8.8	(c)	6.9	8.0
SOL2007-12-14T15:54:15	B8.8	(d)	6.9	2.0
SOL2007-12-14T01:39:20	B9.6	(a)	6.9	2.0
SOL2007-12-14T14:16:30	C1.1	(b)	6.9	6.0

grated over the line of sight column depth, S , can be expressed as:

$$4\pi I = 0.83 \int G(T, n_e) n_e^2 dS. \quad (2)$$

By assuming the electron density, where n_e is obtained from independent density diagnostic pairs, is constant across each pixel, and calculating the line contribution function, $G(T, n_e)$, at the measured electron density, the column depth is derived (see Milligan (2011) for further details). Since the column emission measure EM_{col} is defined by $EM_{col} = \int n_e^2 dS$, we have combined the electron density and column depth measurements to estimate EM_{col} for each diagnostic line pair at the footprint in Event (b).

The 5 panels in Figure 7 show maps of column emission measure for Mg VII, Si X, Fe XII, Fe XIII, and Fe XIV. In each of the five rasters, higher column emission measures were found at the footprint locations compared to the surrounding active region, even in the cooler Mg VII and Si X lines. The footprint column emission measures returned from Figure 7 are between $10^{28} - 10^{29} \text{cm}^{-5}$, in agreement with the regularized inversion method. Uncertainties in both the density estimates and regularized EMDs make it difficult to comment on deviations between the techniques of less than an order of magnitude. However, as the observed deviations are not larger than this, the column emission measures found using line diagnostics do help to reinforce the emission measures obtained via the inversion method.

6. Discussion

Different theoretical models of energy inputs and losses, during flares and in the quiet Sun, pro-

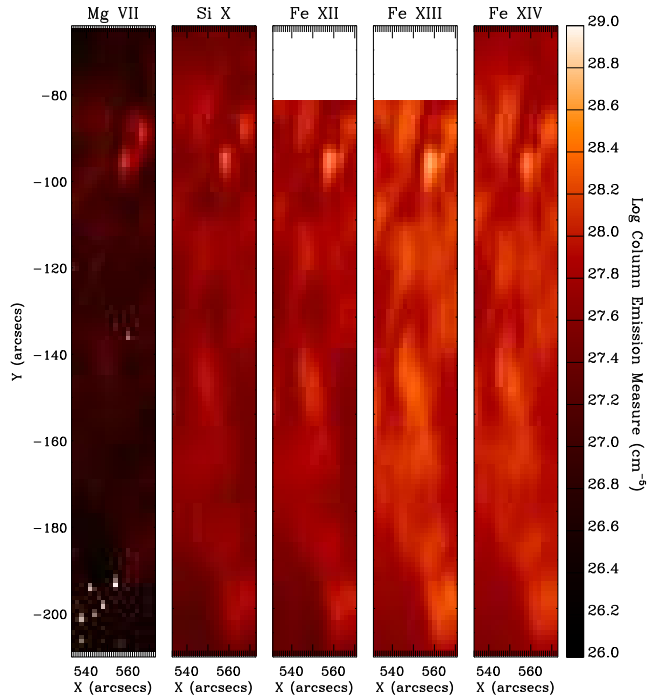


Fig. 7.— The reconstructed column emission measures in Event (b), found by combining the measured electron densities and column depths for the Mg VII, Si X, Fe XII, Fe XIII, and Fe XIV lines. The footprint can be seen at $(-90'' \ 560'')$.

duce EMDs with different slopes, and the slope may provide a diagnostic of the energy balance of the emitting plasma. During a flare the energy balance equation can be very complex, so it is normal to make certain simplifying assumptions - for example, that the temperature and ionization fraction of the plasma has reached a steady

state, that the plasma is gravitationally stratified, and that the emitting structure has constant cross-section. One of the earliest treatments by Shmeleva & Syrovatskii (1973) investigated a flare atmosphere split into two layers. In the upper (high temperature) layer, flare energy deposition occurred, and was balanced by conductive losses to the lower layer. Conduction was assumed to dominate radiative output from this layer. In the lower layer, which did not receive any direct flare heating (e.g. by electrons), the balance was between conductive input from above and radiative losses.

Interpreting Figure 5 in Shmeleva & Syrovatskii (1973), the resulting EMD gradient in a $\log EM - \log T$ plot using a constant pressure assumption was ~ 1.2 over a range of a few $\times 10^5$ to 10^7 K. (It is ~ 2.2 using a constant density assumption). They argue that constant pressure was a valid assumption when dealing with the narrow (compared to pressure scale height) high-temperature transition between the flaring chromosphere and corona.

A similar analysis in Widing (1982), looking only at the layer where conduction and radiation balance, demonstrated a $\log EM - \log T$ slope of 1, as we observed. The difference between this result and that of Shmeleva & Syrovatskii (1973) may lie in the form of the radiative loss function adopted.

The agreement between the slopes found by Shmeleva & Syrovatskii (1973), Widing (1982), and those derived from our observations, is intriguing. Perhaps it suggests that in our events energy injected at the footpoints is localized to the very top of the flare chromosphere, in a region at a temperature of $\log T \gtrsim 6.9$, with the temperature structure beneath determined primarily by conduction and radiation. In other words, any direct flare energy input in the region $\log T \sim 5.5 - 6.9$ is negligible in magnitude compared to other energy loss or gain terms. Brosius (2012) has inferred similar behaviour in a C6.6 class flare. The early appearance of coronal Fe XIX emission and late rise of transition region lines (O V, Si XII and He I) was interpreted as evidence for transition region plasma being heated by thermal conduction from directly heated coronal plasma.

However the agreement between model and observation may also be coincidental, as there are

other assumptions in the analyses discussed. For example, it is assumed that conduction is determined by classical Spitzer conductivity, but the strong temperature gradients implied by the small vertical extent of the flare transition region mean that non-local or saturated flux effects may be important (e.g. Battaglia et al. 2009). Mechanical energy loss and enthalpy flux due to plasma flows (e.g. evaporation) are also neglected. These loss terms may not be important everywhere in the EMD temperature range; Milligan & Dennis (2009) show that in Event (b) high speed evaporative upflows are only present above ~ 2 MK. Underwood et al. (1978) show that the effect of evaporation tends to be to flatten the slope of the EMD. Further work is needed to understand the effects of relaxing these assumptions, as well as on exploring other descriptions for the flare direct energy input and the radiative loss function.

7. Conclusions

We have obtained the first emission measure distribution of the plasma at a flare footpoint using data from *Hinode*/EIS in conjunction with a regularized inversion method. The spectral imaging capabilities of EIS allows us to separate the footpoint EUV spectra – therefore EMD – from loop structures; this ambiguity has been a drawback in many previous studies. The resulting footpoint EMDs can be characterized by an emission measure gradient of $EM(T) \sim T$ between $\log T \sim 5.5 - 6.9$ that falls away at higher temperatures, and peak emission measures on the order of $10^{28} - 10^{29} \text{ cm}^{-5}$. The absolute value of emission measure in the EMDs is further confirmed by the use of density-sensitive line ratios to estimate footpoint column emission measures. In previous theoretical work the EMD gradient is found to be sensitive to the energy transfer methods in a heated atmosphere. Our EMD profiles are in rough agreement with a flaring mechanism depositing energy at the top of the flare chromosphere heated to $\log T \gtrsim 6.9$. Deeper layers then radiate the conductive flux received from the hot layer above.

Obtaining reliable measurements of footpoint EMDs is not only of theoretical interest, as they can be used to better estimate synthetic line intensities in flares. This is useful for identifying blends and lines in other instruments such as the

SDO/EVE spectrometer, or in calibrating instrumental responses for future instruments (see the forthcoming IRIS mission).

The next step in understanding the heating of footpoint plasma is naturally to use RHESSI HXR observations to estimate the energy deposited in the chromosphere. How does the EMD depend on the HXR spectra of the event, are they as consistent as the EMD themselves? Combined with the temperature response in EUV lines a fuller picture would be available to compare various flare heating models.

The authors thank Hugh Hudson and Peter Young for their insightful comments and discussions. We are also grateful to an anonymous referee whose comments led to new insight in interpreting the EMDs. This work was supported by STFC grant ST/I001808/1, by Leverhulme grant F00-179A and by EC-funded FP7 project HESPE (FP7-2010-SPACE-1-263086). DRG acknowledges support from an STFC-funded PhD studentship and ROM is grateful to the Leverhulme Trust for financial support from grant F/00203/X, and to NASA for LWS/TR&T grant NNX11AQ53G. LF & ROM are grateful to ISSI being where the early stages of this work were explored. CHIANTI is a collaborative project involving the NRL (USA), the Universities of Florence (Italy) and Cambridge (UK), and George Mason University (USA). We are grateful for the open data policies of *Hinode* and the efforts of the instrument and software teams. *Hinode* is a Japanese mission developed and launched by ISAS/JAXA, with NAOJ as domestic partner and NASA and STFC (UK) as international partners. It is operated by these agencies in co-operation with ESA and NSC (Norway).

REFERENCES

- Acton, L., Tsuneta, S., Ogawara, Y., et al. 1992, *Science*, 258, 618
- Athay, R. G. 1994, *ApJ*, 423, 516
- Battaglia, M., Fletcher, L., & Benz, A. O. 2009, *A&A*, 498, 891
- Bloomfield, D. S., Mathioudakis, M., Christian, D. J., Keenan, F. P., & Linsky, J. L. 2002, *A&A*, 390, 219
- Bradshaw, S. J. 2009, *A&A*, 502, 409
- Brosius, J. W. 2012, *ApJ*, 754, 54
- Bryans, P., Landi, E., & Savin, D. W. 2009, *ApJ*, 691, 1540
- Culhane, J. L., Harra, L. K., James, A. M., et al. 2007, *Sol. Phys.*, 243, 19
- Del Zanna, G., Mitra-Kraev, U., Bradshaw, S. J., Mason, H. E., & Asai, A. 2011, *A&A*, 526, A1
- Dere, K. P., & Cook, J. W. 1979, *ApJ*, 229, 772
- Dere, K. P., Horan, D. M., & Kreplin, R. W. 1977, *ApJ*, 217, 976
- Dere, K. P., Landi, E., Mason, H. E., Monsignori Fossi, B. C., & Young, P. R. 1997, *A&AS*, 125, 149
- Doschek, G. A., Feldman, U., & Rosenberg, F. D. 1977, *ApJ*, 215, 329
- Feldman, U., Dammasch, I., Landi, E., & Doschek, G. A. 2004, *ApJ*, 609, 439
- Feldman, U., Dorschek, G. A., & Rosenberg, F. D. 1977, *ApJ*, 215, 652
- Feldman, U., Mandelbaum, P., Seely, J. F., Doschek, G. A., & Gursky, H. 1992, *ApJS*, 81, 387
- Fludra, A., & Sylwester, J. 1986, *Sol. Phys.*, 105, 323
- Golub, L., Deluca, E., Austin, G., et al. 2007, *Sol. Phys.*, 243, 63
- Graham, D. R., Fletcher, L., & Hannah, I. G. 2011, *A&A*, 532, A27
- Grevesse, N., & Sauval, A. J. 1998, *Space Sci. Rev.*, 85, 161
- Handy, B. N., Acton, L. W., Kankelborg, C. C., et al. 1999, *Sol. Phys.*, 187, 229
- Hannah, I. G., & Kontar, E. P. 2012, *A&A*, 539, A146
- Hudson, H. S., Strong, K. T., Dennis, B. R., et al. 1994, *ApJ*, 422, L25
- Kashyap, V., & Drake, J. J. 1998, *ApJ*, 503, 450

- Ko, Y.-K., Doschek, G. A., Warren, H. P., & Young, P. R. 2009, *ApJ*, 697, 1956
- Krucker, S., Hudson, H. S., Jeffrey, N. L. S., et al. 2011, *ApJ*, 739, 96
- Landi, E., Del Zanna, G., Young, P. R., Dere, K. P., & Mason, H. E. 2012, *ApJ*, 744, 99
- Leibacher, J., Sakurai, T., Schrijver, K., & van Driel-Gesztelyi, L. 2010, *Sol. Phys.*, 263, 1
- Machado, M. E., & Emslie, A. G. 1979, *ApJ*, 232, 903
- Mazzotta, P., Mazzitelli, G., Colafrancesco, S., & Vittorio, N. 1998, *A&AS*, 133, 403
- McTiernan, J. M., Kane, S. R., Loran, J. M., et al. 1993, *ApJ*, 416, L91
- Milligan, R. O. 2011, *ApJ*, 740, 70
- Milligan, R. O., & Dennis, B. R. 2009, *ApJ*, 699, 968
- Monsignori Fossi, B. C., & Landini, M. 1991, *Advances in Space Research*, 11, 281
- Mrozek, T., & Tomczak, M. 2004, *A&A*, 415, 377
- Neupert, W. M. 1968, *ApJ*, 153, L59+
- O'Dwyer, B., Del Zanna, G., Mason, H. E., Weber, M. A., & Tripathi, D. 2010, *A&A*, 521, A21
- Shmeleva, O. P., & Syrovatskii, S. I. 1973, *Sol. Phys.*, 33, 341
- Tikhonov, A. N. 1963, *Soviet Math. Dokl.*, 4, 1035
- Underwood, J. H., Feldman, U., Dere, K. P., & Antiochos, S. K. 1978, *ApJ*, 224, 1017
- Watanabe, T., Hara, H., Sterling, A. C., & Harra, L. K. 2010, *ApJ*, 719, 213
- Widing, K., & Hiei, E. 1984, *ApJ*, 281, 426
- Widing, K. G. 1982, *ApJ*, 258, 835
- Widing, K. G., & Spicer, D. S. 1980, *ApJ*, 242, 1243